Monthly Notices
of the
ROYAL ASTRONOMICAL SOCIETY

MNRAS **482,** 1706–1714 (2019)
Advance Access publication 2018 October 22

doi:10.1093/mnras/sty2814

Diagnosing solar wind origins using *in situ* measurements in the inner heliosphere

D. Stansby [1]★ T. S. Horbury [1] and L. Matteini[2]

[1]*Department of Physics, Imperial College London, London SW7 2AZ, UK*
[2]*LESIA, Observatoire de Paris, Université PSL, CNRS, Sorbonne Université, Univ. Paris Diderot, Sorbonne Paris Cité, 5 place Jules Janssen, F-92195 Meudon, France*

Accepted 2018 October 15. Received 2018 October 10; in original form 2018 September 24

ABSTRACT

Robustly identifying the solar sources of individual packets of solar wind measured in interplanetary space remains an open problem. We set out to see if this problem is easier to tackle using solar wind measurements closer to the Sun than 1 au, where the mixing and dynamical interaction of different solar wind streams is reduced. Using measurements from the *Helios* mission, we examined how the proton core temperature anisotropy and cross-helicity varied with distance. At 0.3 au there are two clearly separated anisotropic and isotropic populations of solar wind that are not distinguishable at 1 au. The anisotropic population is always Alfvénic and spans a wide range of speeds. In contrast the isotropic population has slow speeds, and contains a mix of Alfvénic wind with constant mass fluxes and non-Alfvénic wind with large and highly varying mass fluxes. We split the *in situ* measurements into three categories according these observations, and suggest that these categories correspond to wind that originated in the core of coronal holes, in or near active regions or the edges of coronal holes, and as small transients form streamers or pseudo-streamers. Although our method by itself is simplistic, it provides a new tool that can be used in combination with other methods for identifying the sources of solar wind measured by *Parker Solar Probe* and *Solar Orbiter*.

Key words: Sun: heliosphere – solar wind.

1 INTRODUCTION

The solar wind is a continuous flow of plasma, travelling away from the Sun to fill interplanetary space. Although well studied by both *in situ* and remote sensing instruments, robustly determining the solar origin of all the solar wind measured *in situ* by spacecraft is still an open problem. Excluding large ejecta, the solar wind has traditionally been classified according to the average speed of protons, which make up ∼95–99 per cent of the wind by ion number density. It is well known that the solar source of fast solar wind ($v > \sim 500\,\mathrm{km\,s^{-1}}$) is open field lines rooted in coronal holes on the surface of the Sun (Krieger, Timothy & Roelof 1973; Sheeley, Harvey & Feldman 1976; Cranmer 2009), and that it is composed of a slowly varying bulk speed superposed with shorter time-scale Alfvénic velocity fluctuations above this background level (Belcher & Davis 1971; Thieme, Schwenn & Marsch 1989; Matteini et al. 2015). The Alfvénic fluctuations are believed to be generated close to the surface of the Sun where the wind is sub-Alfvénic, and then propagate outwards into the heliosphere on long-lived open magnetic field lines (Belcher & Davis 1971; Cranmer & van Ballegooijen 2005). In addition to the global dynamics, the local kinetic properties of fast solar wind are also well known: the protons in fast solar wind have large temperature anisotropies and a low plasma β in the inner heliosphere (Marsch et al. 1982b; Marsch, Ao & Tu 2004; Matteini et al. 2007). In addition, alpha particles, which constitute 1–5 per cent of the solar wind by ion number density, exhibit large magnetic field aligned drifts relative to the protons in the fast solar wind (Marsch et al. 1982a; Steinberg et al. 1996).

In contrast to the fast wind, the plasma properties of the slow solar wind ($v < \sim 500\,\mathrm{km\,s^{-1}}$) are much more variable (Schwenn 2007), and although it must have a number of different solar sources (Abbo et al. 2016), it is not clear how these sources contribute to the different parts of the slow solar wind measured *in situ*. In general there are two possible generation mechanisms for the slow wind: it can flow continuously on magnetic field lines that maintain a connection from the base of the corona to the heliosphere, in

★ E-mail: david.stansby14@imperial.ac.uk

a similar manner to the fast solar wind (Wang & Sheeley 1990; Cranmer, van Ballegooijen & Edgar 2007; Wang 2010), or can be released transiently from closed magnetic field lines undergoing interchange reconnection with the open magnetic field lines that connect to the heliosphere (Sheeley et al. 1997; Einaudi et al. 2001; Rouillard et al. 2010; Higginson et al. 2017).

During initial analysis of *Helios* data, Marsch et al. (1981) discovered a portion of slow solar wind measured at 0.3 au that, apart from its speed, had the same properties of fast solar wind: large proton–alpha drift speeds, large proton core temperature anisotropies, and highly Alfvénic wave activity. In addition, Roberts et al. (1987) described an 80-d interval in the *Helios* data where the purest Alfvénic fluctuations were in slow solar wind. The strong Alfvénic wave activity during these periods implies that the wind was released on open magnetic field lines, allowing the Alfvén waves to freely propagate outwards from the corona to the point of measurement. More recently the presence of an 'Alfvénic slow wind' has been studied statistically using data taken at 1 au, and independent of solar activity the slow solar wind is composed of both non-Alfvénic and Alfvénic components (D'Amicis & Bruno 2015). These results hint that some slow solar wind has exactly the same source (and therefore properties) as fast solar wind, but just happens to be released at a slower speed.

In addition to protons and alphas, much less abundant heavy ions are measured in the solar wind, which can be used as a more direct proxy for solar source than the proton speed. As the solar wind travels away from the Sun it effectively becomes collisionless within a few solar radii (Hundhausen, Gilbert & Bame 1968). This means that ions are no longer able to gain or lose electrons through electron–ion collisions, and the fraction of different charge states become frozen. Ion charge state ratios therefore act as a tracer of the plasma properties at the freezing point. The most commonly used ratios are O^{7+}/O^{6+} and C^{6+}/C^{4+}, which are positively correlated with the electron temperature at the freezing point (Hundhausen et al. 1968; Bochsler 2007; Landi et al. 2012). Low charge state ratios are present in wind that originates in coronal holes, which have relatively low electron temperatures, and high charge state ratios are present in streamer belt plasma that has relatively high electron temperatures. This information can therefore be used to distinguish between coronal hole and non-coronal hole solar wind (Geiss, Gloeckler & Von Steiger 1995; Zhao, Zurbuchen & Fisk 2009). As an example, the Alfvénic slow wind identified by D'Amicis & Bruno (2015) had similar low charge state ratios to the fast solar wind, indicating it had similar solar origins (D'Amicis, Bruno & Matteini 2016), further reinforcing the need to go beyond classifying solar wind based solely on the average proton speed.

Although the *Helios* mission was equipped with an instrument for measuring heavy ions in the solar wind (Rosenbauer et al. 1981), it is believed that the data from this instrument have been lost. However, the case studies of D'Amicis & Bruno (2015) and D'Amicis et al. (2016) hint that when heavy ion measurements are not available the Alfvénicity of the solar wind fluctuations may be a more reliable proxy for solar wind origin than speed. The problem with using Alfvénicity as a categorization variable is that the solar wind becomes systematically less Alfvénic with distance (Roberts et al. 1987; Bruno et al. 2007; Iovieno et al. 2016) due to both small-scale turbulent evolution and large-scale velocity shears and interaction regions (Bruno et al. 2006). This means not all solar wind that started off Alfvénic near the Sun is still Alfvénic when it is measured at 1 au. In this paper, we mitigate this problem by using the unique *Helios* data, with measurements of solar wind plasma from 0.3 to 1 au, to link properties measured *in situ*, that are only observable at distances <1 au, to solar sources. The *Helios* data are described in Section 2, and statistical results are presented in Section 3. Based on these observations we construct three different categories of solar wind, and in Section 4 we place possible solar sources to each of these categories. In Section 5, we compare our categorization scheme with other schemes, and then conclude and present a set of predictions for the upcoming *Solar Orbiter* and *Parker Solar Probe* missions in Section 6.

2 DATA

The data used here were measured by the twin *Helios* spacecraft, which were operational during the late 1970s and early 1980s. Both spacecraft had an electrostatic analyser for measuring the ion distribution function at 40.5 s cadence (Schwenn, Rosenbauer & Miggenrieder 1975), and two different fluxgate magnetometers for measuring the magnetic field (Musmann et al. 1975; Scearce et al. 1975). Here we use a reanalysis of the ion distribution functions that fitted a bi-Maxwellian to the proton core population present in the experimentally measured ion distribution functions. This data set provides the proton core number density (n_p), velocity ($\boldsymbol{v}_p$), temperatures parallel ($T_{p_\parallel}$), and perpendicular ($T_{p\perp}$) to the magnetic field, and corresponding magnetic field values ($\boldsymbol{B}$) at a maximum cadence of 40.5 s. For more details on the fitting procedure and access to the data see Stansby et al. (2018a). Note that all the data presented in this paper are parameters of the proton core population, and not numerical moments of the overall ion distribution. The total temperature was calculated as $T_p = (2T_{p\perp} + T_{p\parallel})/3$, the temperature anisotropy as $T_{p\perp}/T_{p_\parallel}$, the parallel plasma β as $\beta_p = 2\mu_0 n_p k_B T_{p\parallel}/|\boldsymbol{B}|^2$, and the Alfvén speed as $v_A = |\boldsymbol{B}|/\sqrt{n_p m_p \mu_0}$.

To avoid contamination of very large transients all of the intervals listed as coronal mass ejections by Liu, Richardson & Belcher (2005) were removed from the data set before further analysis. The state of the Sun undergoes an 11-yr solar cycle, oscillating between solar minimum and solar maximum. Because the highest quality *Helios* data were taken early in the mission, only data taken in the years 1974–1978 inclusive (during the solar minimum between cycles 20 and 21) were used.

2.1 Alfvénicity

In order to classify the solar wind as Alfvénic or non-Alfvénic, the cross-helicity was calculated in every 20-min interval where at least 10 velocity and magnetic field data points were available. The cross-helicity is defined as

$$\sigma_c = 2\frac{\langle \boldsymbol{v}\cdot\boldsymbol{b}\rangle}{\left\langle |\boldsymbol{v}|^2 + |\boldsymbol{b}|^2\right\rangle}, \tag{1}$$

where $\boldsymbol{v} = \boldsymbol{v}_p - \boldsymbol{v}_{p0}$ are the proton velocity fluctuations in the wave frame, $\boldsymbol{v}_{p0}$ is the local Alfvén wave phase velocity, $\boldsymbol{b} = v_A(\boldsymbol{B}/|\boldsymbol{B}|)$ is the magnetic field in velocity units, and $\langle\rangle$ indicates a time average over all points in a 20-min interval (Bruno & Carbone 2013). $\boldsymbol{v}_{p0}$ was calculated using the method given by Sonnerup et al. (1987), which finds the local de-Hoffman Teller frame of reference in which $\left\langle|\boldsymbol{v}\times\boldsymbol{b}|^2\right\rangle$ is minimized; by construction, this is the value of $\boldsymbol{v}_{p0}$ for which the absolute value of σ_c is maximized. Although a plasma with Alfvén waves propagating in opposite directions can have low values of σ_c, in this paper 'Alfvénic' is specifically reserved to denote a plasma where Alfvén waves propagate predominantly in only one direction.

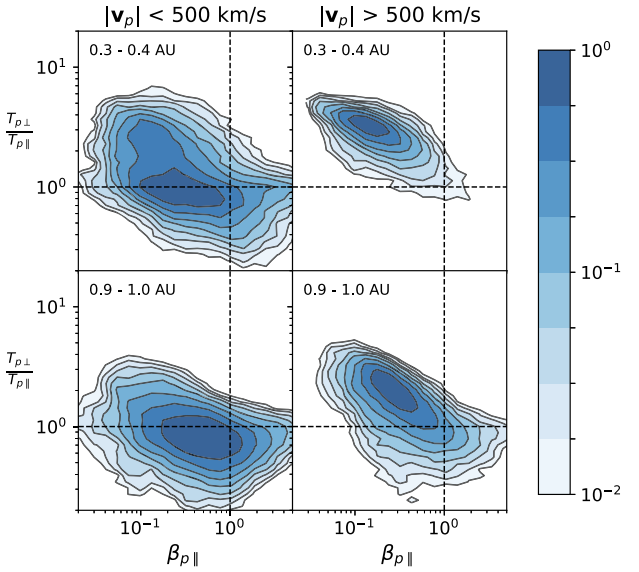

Figure 1. Distribution of data in the $\beta_{p\parallel}$–$T_{p\perp}/T_{p\parallel}$ plane. Contours are interpolated from 2D histogram counts with 40 bins logarithmically spaced along each axis and normalized to the maximum bin count. Left-hand panels show slow solar wind and right-hand panels show fast solar wind. Top panels show the distribution at 0.3–0.4 au and bottom panels show 0.9–1.0 au.

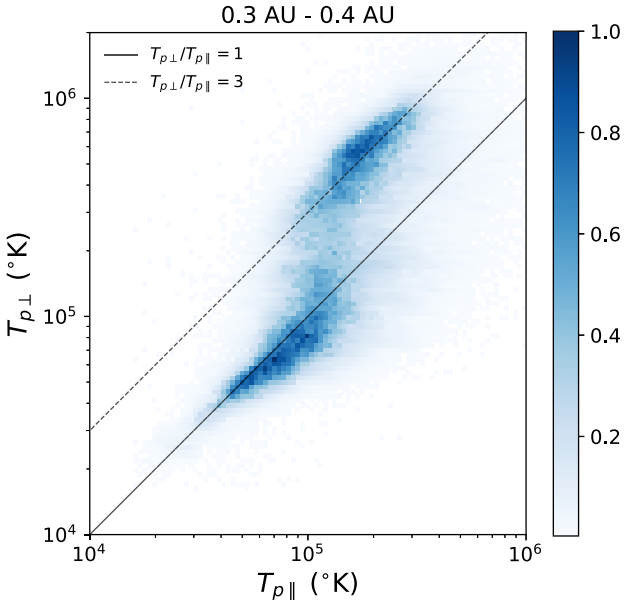

Figure 2. Joint probability distribution of parallel and perpendicular proton temperatures at 0.3–0.4 au. Histogram values are bin counts normalized to the maximum bin value. In this parameter space lines of constant temperature anisotropy are diagonal with a gradient of 1, with two examples shown for reference.

The magnitude of σ_c indicates whether the fluctuations in the plasma are predominantly unidirectional Alfvén waves ($|\sigma_c| \approx 1$) or not ($|\sigma_c| < 1$). For Alfvénic periods, the sign of σ_c determines the direction of wave propagation with respect to the local magnetic field. Because Alfvén waves in the solar wind almost always travel away from the Sun (Gosling et al. 2009), the sign of σ_c is a reliable proxy for the magnetic polarity of the solar wind.

2.2 Entropy

Heavy ion charge state data measured at 1 au is commonly used to diagnose the solar origin of solar wind. Unfortunately there is no heavy ion data available from the *Helios* mission, so instead proton specific entropy was used as a proxy. The specific entropy argument is easily calculated from the proton distribution parameters and given by

$$S_p = T_p n_p^{\alpha-1}, \tag{2}$$

where α is the polytropic index of the fluid. Here α was taken to be 1.5, the value used by Pagel et al. (2004) and Stakhiv et al. (2016) who studied correlations between entropy and composition, and whose results are used in Section 4.2 to make an indirect link between proton temperature anisotropy and heavy ion charge states using S_p as an intermediate variable.

3 RESULTS

3.1 Statistics

Fig. 1 shows the distribution of the solar wind in the $\beta_{p\parallel}$–$T_{p\perp}/T_{p\parallel}$ plane measured by *Helios* at heliocentric distances of 0.3–0.4 and 0.9–1.0 au, and split into slow and fast wind using a simple cut in speed. The distribution at 0.3 au has previously been presented for an individual high speed stream by Matteini et al. (2007). The top right-hand panel of Fig. 1 shows that the ∼100-h continuous high speed stream in Matteini et al. (2007) is representative of all 542 h of fast solar wind measured by *Helios* at 0.3 au during solar minimum. The distribution at 1 au is also well known, and the *Helios* data measured in the years 1974–1978 (bottom two panels of Fig. 1) agrees well with data from the *WIND* spacecraft measured from 1995 to 2012 (e.g. Maruca, Kasper & Bale 2011). As the wind propagates outwards the protons become more isotropic and the plasma β increases, primarily due to adiabatic evolution (Chew, Goldberger & Low 1956; Matteini et al. 2011), although by 1 au the fast wind protons have not yet reached the equilibrium state of $T_{p\perp}/T_{p\parallel} = 1$. In contrast, at 1 au the slow solar wind is distributed around $T_{p\perp}/T_{p\parallel} = 1$, where it is thought to be maintained during transit by a combination of collisions and kinetic instabilities that are active when $\beta_{p\parallel} \geq 1$ (e.g. Kasper, Lazarus & Gary 2002; Hellinger et al. 2006; Bale et al. 2009; Yoon 2016).

At 0.3 au the majority of the slow solar wind is also spread around $T_{p\perp}/T_{p\parallel} = 1$, but there is a significant fraction with $T_{p\perp}/T_{p\parallel} > 2$ and $\beta_p \ll 1$ (Fig. 1, top left). This is the same region in the parameter space that fast solar wind occupies at 0.3 au, which implies that there is a portion of slow solar wind that has the same kinetic properties as fast solar wind. Instead of partitioning the data by speed, Fig. 2 shows the joint distribution of $T_{p\perp}$ and $T_{p\parallel}$ for all measurements between 0.3 and 0.4 au. In this parameter space two populations are clearly distinct: one centred around $T_{p\perp}/T_{p\parallel} = 1$ and other centred around $T_{p\perp}/T_{p\parallel} = 3$. All fast solar wind occupies the anisotropic population, but the slow wind is split between the two populations (as shown in Fig. 1).

In addition to being anisotropic, the fast solar wind is filled by antisunward propagating Alfvén waves. This is a statement about the global dynamics of the plasma, in contrast to the local kinetic properties given by the parallel and perpendicular temperatures, and is a consequence of the wind being released on long-lived open field lines. To investigate whether the anisotropic wind as a whole has the same Alfvénic property as the fast solar wind, Fig. 3 shows the joint

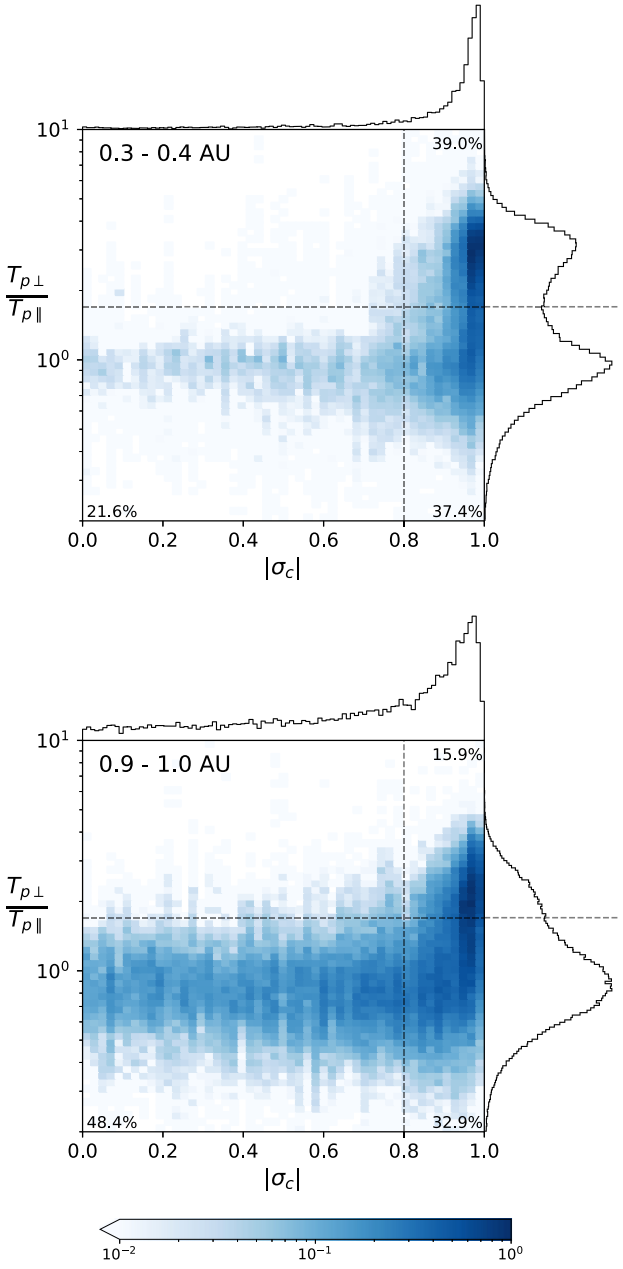

Figure 3. 2D histograms of temperature anisotropy against absolute cross-helicity (main panels) with adjoining 1D histograms of temperature anisotropy (right-hand panels) and cross-helicity (top panels). 2D bin counts are normalized to the maximum bin count. 1D histograms are linearly scaled. The horizontal and vertical dashed lines show the partitioning of the parameter space into three distinct regions; see text in Section 3.1 for more details. Percentages indicate the fraction of data points in each of the three regions.

probability distribution of temperature anisotropy and cross-helicity at both 0.3 and 1 au. The distribution of temperature anisotropy is clearly bimodal at 0.3 au with a minimum at $T_{p\perp}/T_{p_\parallel} = 1.7$, a feature that is not observable at 1 au due to the 0.3 au anisotropic component becoming more isotropic with radial distance (as a result of adiabatic evolution). The distribution stops being clearly bimodal at radial distances greater than around 0.8 au (not shown). In the rest of this paper data taken at 0.3–0.4 au are presented, but the qualitative properties discussed are present at all radial distances from 0.3 to 0.8 au.

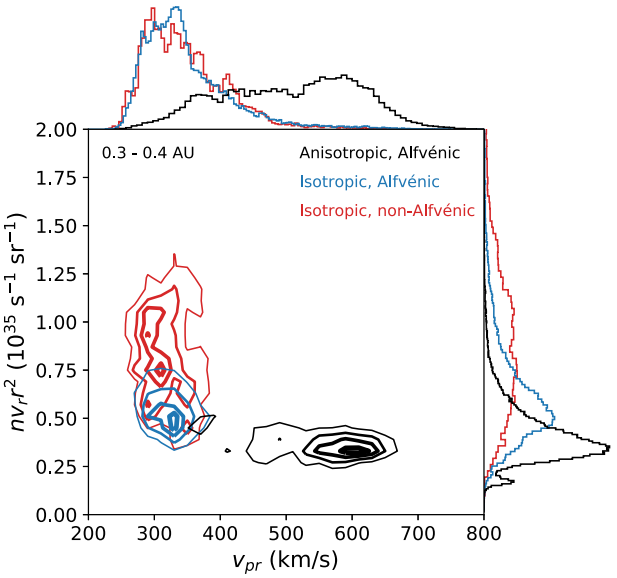

Figure 4. Contours of the 2D histograms of radial number density flux against radial velocity (centre panel) with adjoining 1D histograms of radial velocity (top panel) and radial number density flux (right-hand panel) from data taken at 0.3–0.4 au. Different colours represent the three different categories of solar wind defined statistically in the top panel of Fig. 3. Contours are interpolated from a 2D histogram and plotted at levels of (0.3, 0.5, 0.7, and 0.9) times the maximum bin value. 1D histograms are linearly scaled.

It is clear from Fig. 3 that the fraction of solar wind that is Alfvénic is much higher at 0.3 au (∼80 per cent) as compared with 1 au (∼50 per cent), which agrees well with previous studies (Roberts et al. 1987; Bruno et al. 2007). At 0.3 au the anisotropic population is almost always Alfvénic (i.e. $|\sigma_c| > 0.8$), but this is not the case for the isotropic wind. We therefore propose splitting the solar wind at 0.3 au into three populations based on the observable boundaries in this parameter space:

(i) an anisotropic, Alfvénic population;
(ii) an isotropic, Alfvénic population;
(iii) an isotropic, non-Alfvénic population.

The split in anisotropy was chosen to be the saddle in between the two populations at $T_{p\perp}/T_{p_\parallel} = 1.7$, and the split in cross-helicity was chosen at the edge of the Alfvénic population at $|\sigma_c| = 0.8$. These boundaries are shown in Fig. 3. At 0.3–0.4 au, ∼80 per cent of the wind was Alfvénic, split equally between isotropic and anisotropic, and the remaining 20 per cent was non-Alfvénic.

With this classification in mind, the top panel of Fig. 4 shows the radial velocity distribution of the solar wind in each category. Both isotropic populations consist primarily of solar wind with speeds less than 500 km s^{-1}, whereas the anisotropic population spans a wide range of speeds from 300 to 700 km s^{-1}. In fact, at 0.3–0.4 au *Helios* measured slightly more anisotropic solar wind below 500 km s^{-1} than above. This reinforces the idea that the concept of fast and slow solar winds breaks down at intermediate speeds where wind can have properties similar to either the very slow or very fast wind, and again suggests that some slow wind may have the same origin as fast wind. Another known property of the fast solar wind is that the radial mass flux does not depend on speed (Feldman et al. 1978; Wang 2010). To investigate whether this is true for the anisotropic wind as a whole, the main panel of Fig. 4 shows radial flux as a function of radial velocity for each of the

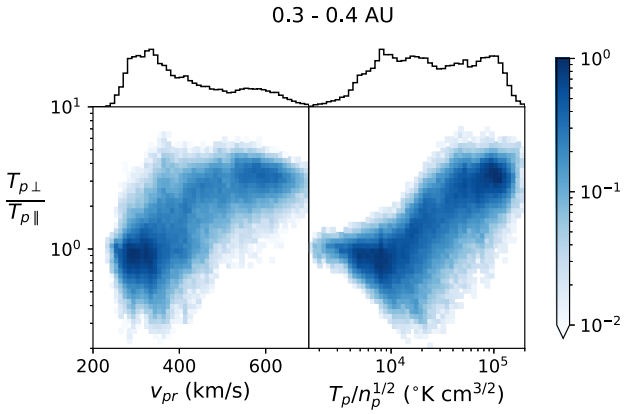

Figure 5. Joint probability distributions of temperature anisotropy (*y*-axis) against radial velocity (*x*-axis, left-hand panel) and proton specific entropy (*x*-axis, right-hand panel). 1D histograms for the *x*-axis variables are shown above the 2D histograms on a linear scale.

three categories. The anisotropic wind has a constant flux that does not depend on speed; when evaluated at 1 au this average flux is $\sim 1.8 \times 10^8\,\mathrm{cm^{-2}\,s^{-1}}$, which agrees well with independent measurements made at 1 au and beyond (Phillips et al. 1995; Goldstein et al. 1996; Wang 2010). The isotropic Alfvénic wind has a slightly higher flux, whereas the non-Alfvénic wind has widely ranging fluxes varying up to 1–4 times the base value of the anisotropic wind, suggesting a distinct physical origin.

To investigate the link between the three categories and their source regions on the Sun, we also looked at the dependence of temperature anisotropy on proton specific entropy (used later as a proxy for composition). Fig. 5 shows the joint distribution of temperature anisotropy, and solar wind speed or proton specific entropy. At 0.3 au, low-speed wind (200–300 km s^{-1}) is all isotropic, and at high speeds (450–700 km s^{-1}) all of the wind is anisotropic, however, at intermediate speeds (300–450 km s^{-1}) the wind is spread between the two different states of $T_\perp/T_\parallel$. In contrast, the variation between temperature anisotropy and specific entropy is slightly smoother; isotropic wind corresponds exclusively to low entropy and anisotropic wind exclusively to high entropy, with a continuous variation in between. This result is used only as a correlation, and we do not claim that there is any causal relationship between entropy and temperature anisotropy. In Section 4.2, we discuss how this correlation can be used as an intermediate step to infer the compositional properties of our three different categories.

3.2 Spatial distribution of the three solar wind populations

We have shown that at 0.3 au it is possible to distinguish between three types of solar wind based on the statistics of proton temperature anisotropy and Alfvénicity. To understand the spatial distribution of each population within the solar wind, Fig. 6 shows the time series measurements made by *Helios 1* inside 0.5 au during its first perihelion pass.

The bimodal nature of proton temperature anisotropy is clear, even within the unaveraged and noisy 40.5-s cadence measurements, and the wind remained in one anisotropy state for days at a time. In contrast, within the isotropic category the Alfvénic and non-Alfvénic subcategories are well mixed and interspersed within each other. During some isotropic periods (e.g. around 1975-03-09) the non-Alfvénic wind is subdominant and appears to be embedded in the Alfvénic wind, whereas at other times (e.g. around 1975-03-30) there appears to be an approximately even mix of Alfvénic and non-Alfvénic wind.

The transition from isotropic to anisotropic wind was sharp, and always occurred at the leading edge of high-speed streams. It is known that composition and entropy undergo sharp changes at the leading edge of high-speed streams (Wimmer-Schweingruber, von Steiger & Paerli 1997; Lazarus et al. 2003; Crooker & McPherron 2012), but Fig. 6 demonstrates that a coincident temperature anisotropy boundary is also present. The sharp increases temperature anisotropy were driven by increases in $T_\perp$, whilst $T_\parallel$ stayed roughly constant across the boundaries (not shown). The transition from anisotropic back to isotropic was also sharp, caused by sharp decreases in $T_\perp$, and occurred inside the rarefaction edge of high-speed streams. The sudden drop in $T_\perp$, which caused a coincident drop in total temperature and therefore a drop in specific entropy, was not correlated with changes in the cross-helicity. The only other observable change in the plasma and magnetic field data are magnetic field fluctuations that look qualitatively different on either side of the boundary (not shown). The time series gives a clear visual demonstration that it is impossible to cut the velocity in a single place to separate different types of wind, but clear bimodality makes a cut in temperature anisotropy easy. We reiterate that performing this separation is only possible at heliocentric distances <0.8 au, as at large distances the anisotropic wind becomes more isotropic, such that the two populations are no longer separable.

4 LINKING *IN SITU* MEASUREMENTS TO SOLAR SOURCES

We now use the observations made in Section 3 to link our three categories of solar wind to their solar sources. A summary of the conclusions drawn in this section is given in Table 1.

4.1 Known properties of coronal hole wind

It has long been known that wind originating on open field lines rooted inside large coronal holes forms the fast solar wind (Krieger et al. 1973; Sheeley et al. 1976; Cranmer 2009). Remote sensing measurements also show pronounced temperature anisotropies present above coronal holes, whilst the solar wind is still near to the Sun (Kohl et al. 1997; Cranmer, Panasyuk & Kohl 2008). Because the anisotropic category is the only one with high speeds (Fig. 4), we infer that wind produced in the core of coronal holes belongs to our anisotropic category. The spatial distribution of anisotropic wind, with slower speeds always occurring in the rarefaction edges of high-speed streams (Fig. 6), shows that rarefaction during transit is responsible for the relatively low speed of some anisotropic wind (Pizzo 1991). The reason slower speeds are not observable at the leading edge of high-speed streams is because by 0.3 au they have already been accelerated by the faster wind to form a corotating interaction region (Burlaga 1974; Pizzo 1991; McGregor et al. 2011; Richardson 2018).

Note that we have chosen to distinguish between the edges and the core of coronal holes; at the edge of coronal holes the magnetic field lines typically undergo large separations as a function of height in the corona, which has the effect of reducing both the wind speed (Levine, Altschuler & Harvey 1977; Wang & Sheeley 1991; Cranmer et al. 2007; Pinto, Brun & Rouillard 2016) and charge state ratios (Wang, Ko & Grappin 2009). In the next two sections further evidence is used to predict which one of our three categories coronal hole edge wind is part of.

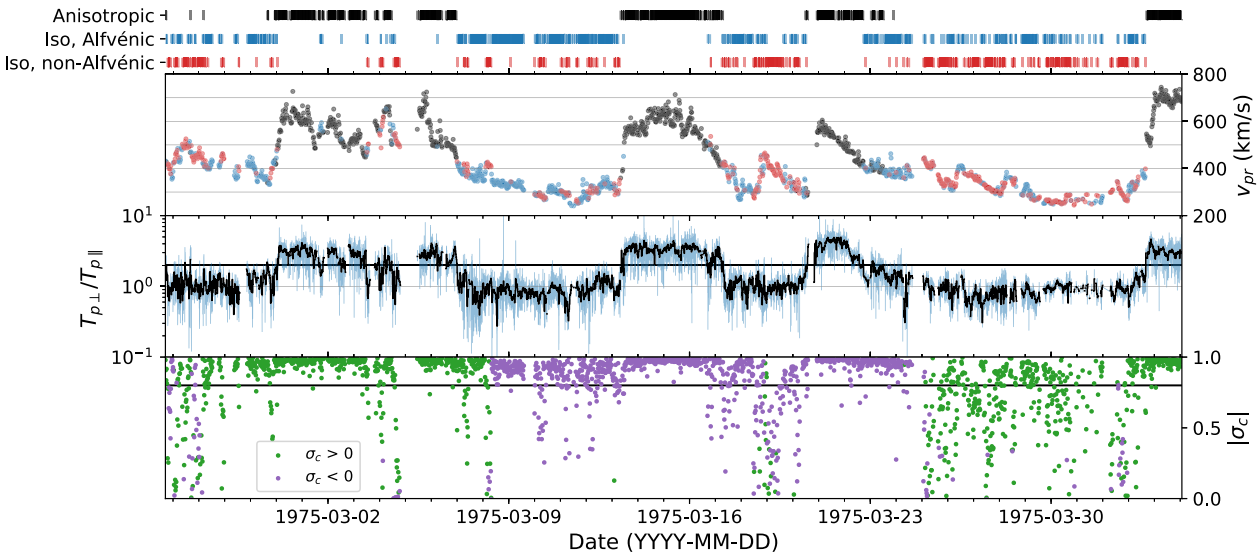

Figure 6. Time series data from the first perihelion pass of *Helios 1*, illustrating the categorization displayed statistically in the top panel of Fig. 3. Top panel shows the categorization. Second panel shows the radial proton speed, coloured by the categorization. Third panel shows full resolution proton temperature anisotropy (light blue) and 20-min averaged values (dark black). The line at $T_{p\perp}/T_{p\parallel} = 1.7$ shows the boundary between anisotropic (points above) and isotropic (points below) wind. Bottom panel shows absolute values of 20-min cross-helicity, coloured by sign. The line at $|\sigma_c| = 0.8$ shows the threshold separating Alfvénic (points above) and non-Alfvénic (points below) wind.

Table 1. Properties of our three categories of solar wind near the Sun at solar minimum. The first six rows show properties directly measured by *Helios* at distances 0.3–0.4 au in this study. The bottom four rows show inferred properties. See Section 4 for more details.

	Isotropic non-Alfvénic	Isotropic Alfvénic	Anisotropic
Fraction at 0.3–0.4 au	21.6%	37.4%	39.0%
Speed	200–500 km s^{-1}	200–500 km s^{-1}	300–700 km s^{-1}
$T_{p\parallel}$	0.02–0.4 MK	0.02–0.4 MK	0.03–0.4 MK
$T_{p\perp}$	0.01–0.1 MK	0.01–0.1 MK	0.1–1 MK
Entropy	Low	Low	High
Mass flux	Variable	Constant	Constant
Coronal freeze in temperature	High	High	Low
O^{7+}/O^{6+}	High	High	Low
C^{6+}/C^{5+}	High	High	Low
Solar source(s)	Small-scale transients	Active regions, coronal hole edges	Coronal hole cores

4.2 Correlation of anisotropy, entropy, and composition

At distances beyond 1 au the proton specific entropy is anticorrelated with the O^{7+}/O^{6+} charge state ratio (Pagel et al. 2004). In addition, observations at 1 au show that specific entropy is anticorrelated with the C^{6+}/C^{4+} charge state ratio (Stakhiv et al. 2016). We have shown in Fig. 5 that entropy has a monotonic dependence on proton temperature anisotropy (but note again that this is not necessarily a causal relationship). Linking this newly observed relationship to the inferred relationship between entropy and charge state ratios suggests that anisotropic wind has low O^{7+}/O^{6+} and C^{6+}/C^{4+} charge state ratios, and isotropic wind has high charge state ratios. In addition to being related statistically, the sharp boundaries between anisotropic wind and isotropic wind mimic the locations of sharp composition boundaries found in other studies (see Section 3.2 for a discussion). This backs up the statistical inference derived between proton temperature anisotropy and heavy ion charge states.

Using specific entropy as a bridge between anisotropy and composition therefore corroborates our previous conclusion that anisotropic wind originates in the core of large coronal holes, which are known to emit wind with low charge state ratios (Geiss et al. 1995; Wang et al. 2009). This allows us to infer that both categories of isotropic wind do not originate in the core of coronal holes, but may originate at coronal hole edges or outside coronal holes. This again agrees with remote sensing measurements that show reduced temperature anisotropies near the edges of coronal holes when compared to the core of coronal holes (Susino et al. 2008). We therefore suggest that the 'isotropic' wind forms what is commonly thought of as the 'slow solar wind'. There are a number of theories as to the origin of the slow solar wind (Abbo et al. 2016); in the next section we assign possible theories to either the Alfvénic or non-Alfvénic categories of the isotropic wind.

4.3 Alfvénicity and mass flux variability

Solar wind with a high Alfvénicity implies a steady state release of plasma on open field lines. This hypothesis is supported by the relatively constant mass flux in the Alfvénic isotropic wind (see Fig. 4). This means any Alfvénic wind must have been released on

field lines that remained open for at least the 20-min resolution of the cross-helicity calculated from *in situ* data. Areas of long lasting open field on the Sun can be split into the core of coronal holes (already categorized), edges of coronal holes, and active regions. Remote sensing measurements have shown that active region outflows have high coronal electron temperatures (Neugebauer et al. 2002; Brooks & Warren 2012), contain open field lines allowing plasma to escape into the heliosphere (Slemzin et al. 2013), and can supply mass fluxes similar to those measured *in situ* (Brooks, Ugarte-Urra & Warren 2015). We therefore conclude active region wind is most consistent with the isotropic Alfvénic category, along with the wind from the edges of coronal holes that also contain long lasting open magnetic fields and has similar properties.

Finally, we predict that the non-Alfvénic wind is consistent with the final known type of slow solar wind, typically called 'number density structures' or 'blobs', which have been detected both remotely (e.g. Sheeley et al. 1997; Viall & Vourlidas 2015; DeForest et al. 2018) and *in situ* (e.g. Kepko & Spence 2003; Sanchez-Diaz et al. 2017; Stansby & Horbury 2018). These are non-steady state transient structures with a high density but similar speed as the surrounding slow wind, and therefore have enhanced mass fluxes relative to the background wind. This property is exactly what we have measured for the non-Alfvénic wind (Fig. 4), backing up our final categorization.

A summary of our mapping of possible solar sources to *in situ* solar wind categories is given in Table 1.

5 COMPARISON WITH OTHER CATEGORIZATION SCHEMES

Recently several authors have also attempted to categorize sources of the solar wind using *in situ* observations, choosing the categories of coronal mass ejection wind, coronal hole wind, and interstream wind (for a summary, see Neugebauer, Reisenfeld & Richardson 2016). In this paper, we have deliberately removed coronal mass ejection wind from our data set, and have used proton temperature anisotropy as the only variable separating coronal hole wind (anisotropic) and interstream wind (isotropic).

Zhao et al. (2009) used only the O^{7+}/O^{6+} ratio and solar wind speed measured at 1 au. This method is limited by the slow cadence (1 h) of charge state ratio measurements available, but has the advantage that the O^{7+}/O^{6+} ratio is known to be directly related to plasma properties near the Sun. Because the distribution of heavy ion charge states is only clearly bimodal at solar minimum (Zurbuchen et al. 2002), it is not clear if this method works well during solar maximum conditions. Because our method also assumes a bimodal distribution of charge state ratios, it is not clear if it is still applicable during solar maximum conditions either.

Xu & Borovsky (2015) picked *in situ* measurements, manually categorized specific intervals of the measurements, and then tried to find boundaries in a multidimensional parameter space that reliably split the data into the assumed categories. These boundaries could then be applied to other intervals where the categorization is unknown. This method is practical and pragmatic for rapidly categorizing solar wind sources, but the boundaries between categories are somewhat arbitrary and do not necessarily directly relate to the different physics of solar wind formation at each solar wind source. The advantage of the Xu & Borovsky (2015) method is that it only uses single-point measurements of solar wind protons and magnetic fields, so the cadence at which it can be applied is limited only by that of the *in situ* measurements. In contrast our method is limited to a 20-min cadence, which is in practice limited by the number of 40.5-s cadence of proton measurements needed to reliably calculate σ_c.

Other authors have backmapped solar wind measured at 1 au to try and determine the exact location on the Sun from which it originated (e.g. Neugebauer et al. 1998; Fu et al. 2015; Fazakerley, Harra & van Driel-Gesztelyi 2016; Peleikis et al. 2017; Zhao et al. 2017). This method assumes that the solar wind travels along magnetic field lines between the Sun's surface and magnetic field source surface at $2.5r_s$ (solar radii), which are computed using a potential field source surface model, and then travels radially and at a constant speed to the *in situ* observer. This method has the advantage of drawing a direct link by trying to predict the exact solar wind source location of *in situ* measurements. Although it is successful in identifying sources on very large time-scales of ∼days, it is currently not possible to probe smaller scales, and does not take into account dynamical processing that occurs during transit between the Sun and the *in situ* observer.

6 CONCLUSIONS AND PREDICTIONS FOR FUTURE MISSIONS

We have presented an attempt to map *in situ* measurements of solar wind to their sources, using properties of the solar wind observable at 0.3 au that are unobservable at 1 au due to dynamical interactions during transit. We find that the solar wind can be split into three categories (summarized in Table 1), based on *in situ* measurements of proton temperature anisotropy and Alfvénicity (Section 3), and sort possible solar origins of the solar wind into these three categories (Section 4). Although many other methods have been developed to attempt the same goal of solar source categorization (Section 5), the lack of *in situ* composition and remote sensing data available during the *Helios* era (1974–1984) restricted our ability to use these more modern techniques. However, in the near future we will have access to simultaneous *in situ* measurements of protons in the inner heliosphere, *in situ* measurements of solar wind composition, and a wide range of remote sensing data. We finish by describing how our new categorization scheme can be applied to data from upcoming missions to the inner heliosphere.

Parker Solar Probe (*PSP*; Fox et al. 2016) will make *in situ* measurements of the solar wind at heliocentric distances inside 0.3 au, and the first comprehensive *in situ* solar wind measurements inside 1 au since *Helios*. Proton and magnetic field measurements made by *PSP* will allow us to perform the categorization scheme outlined in this paper. Advances in modelling and remote sensing since the *Helios* era mean that it will then be possible to backmap the solar wind measured by *PSP* to a predicted source location on the Sun. If our categorization is correct, the three categories of *in situ* solar wind will backmap to their respective inferred solar sources.

Solar Orbiter (*SO*; Müller et al. 2013) will provide the first solar wind composition measurements between 0.3 and 1 au. This will allow us to directly test the correlation between temperature anisotropy and charge state ratios, without having to bridge the gap by using proton specific entropy as an intermediate variable. If our categorization is correct, isotropic wind will clearly correspond to high charge state ratios, and anisotropic wind will clearly correspond to low charge state ratios. In addition *SO* will carry on board remote sensing instruments that are designed to target the predicted solar sources of *in situ* measurements, making backmapping wind to its source even more accurate than using remote sensing instruments at 1 au.

ACKNOWLEDGEMENTS

DS is supported by STFC studentship ST/N504336/1, and thanks Trevor Bowen, Allan MacNeil, Denise Perrone, and Alexis Rouillard for helpful discussions. TSH is supported by STFC grant ST/N000692/1. This work was supported by the Programme National PNST of CNRS/INSU cofunded by CNES.

Data were retrieved using HELIOPY v0.5.3 (Stansby, Yatharth & Shaw 2018b) and processed using ASTROPY v3.0.3 (Astropy Collaboration et al. 2018). Figures were produced using MATPLOTLIB v2.2.2 (Hunter 2007; Droettboom et al. 2018).

Code to reproduce the figures presented in this paper is available at https://github.com/dstansby/publication-code.

REFERENCES

Abbo L. et al., 2016, Space Sci. Rev., 201, 55
Astropy Collaboration et al., 2018, AJ, 156, 123
Bale S. D., Kasper J. C., Howes G. G., Quataert E., Salem C., Sundkvist D., 2009, Phys. Rev. Lett., 103, 211101
Belcher J. W., Davis L., 1971, J. Geophys. Res., 76, 3534
Bochsler P., 2007, A&AR, 14, 1
Brooks D. H., Warren H. P., 2012, ApJ, 760, L5
Brooks D. H., Ugarte-Urra I., Warren H. P., 2015, Nat. Commun., 6, 5947
Bruno R., Carbone V., 2013, Living Rev. Sol. Phys., 10, 1
Bruno R., Bavassano B., D'amicis R., Carbone V., Sorriso-Valvo L., Pietropaolo E., 2006, Space Sci. Rev., 122, 321
Bruno R., D'Amicis R., Bavassano B., Carbone V., Sorriso-Valvo L., 2007, Ann. Geophys., 25, 1913
Burlaga L. F., 1974, J. Geophys. Res., 79, 3717
Chew G. F., Goldberger M. L., Low F. E., 1956, Proc. R. Soc. A: Math. Phys. Eng. Sci., 236, 112
Cranmer S. R., 2009, Living Rev. Sol. Phys., 6, 3
Cranmer S. R., van Ballegooijen A. A., 2005, ApJS, 156, 265
Cranmer S. R., van Ballegooijen A. A., Edgar R. J., 2007, ApJS, 171, 520
Cranmer S., Panasyuk A., Kohl J., 2008, ApJ, 678, 1480
Crooker N. U., McPherron R. L., 2012, J. Geophys. Res.: Space Phys., 117, A09104
D'Amicis R., Bruno R., 2015, ApJ, 805, 84
D'Amicis R., Bruno R., Matteini L., 2016, in Wang L., Bruno R., Möbius E., Vourlidas A., Zank G., eds, AIP Conf. Proc. Vol. 1720, Solar Wind 14: Proceedings of the Fourteenth International Solar Wind Conference. Am. Inst. Phys., New York, p. 040002
DeForest C. E., Howard R. A., Velli M., Viall N., Vourlidas A., 2018, ApJ, 862, 18
Droettboom M. et al., 2018, Matplotlib: Plotting with Python. matplotlib/matplotlib v2.2.2. Available at: https://zenodo.org/record/1202077
Einaudi G., Chibbaro S., Dahlburg R. B., Velli M., 2001, ApJ, 547, 1167
Fazakerley A. N., Harra L. K., van Driel-Gesztelyi L., 2016, ApJ, 823, 145
Feldman W. C., Asbridge J. R., Bame S. J., Gosling J. T., 1978, J. Geophys. Res., 83, 2177
Fox N. J. et al., 2016, Space Sci. Rev., 204, 7
Fu H., Li B., Li X., Huang Z., Mou C., Jiao F., Xia L., 2015, Sol. Phys., 290, 1399
Geiss J., Gloeckler G., Von Steiger R., 1995, Space Sci. Rev., 72, 49
Goldstein B. E. et al., 1996, A&A, 316, 296
Gosling J. T., McComas D. J., Roberts D. A., Skoug R. M., 2009, ApJ, 695, L213
Hellinger P., Trávníček P., Kasper J. C., Lazarus A. J., 2006, Geophys. Res. Lett., 33, L09101
Higginson A. K., Antiochos S. K., DeVore C. R., Wyper P. F., Zurbuchen T. H., 2017, ApJ, 837, 113
Hundhausen A. J., Gilbert H. E., Bame S. J., 1968, ApJ, 152, L3
Hunter J. D., 2007, Comput. Sci. Eng., 9, 90
Iovieno M., Gallana L., Fraternale F., Richardson J. D., Opher M., Tordella D., 2016, European J. Mech. – B/Fluids, 55, 394
Kasper J. C., Lazarus A. J., Gary S. P., 2002, Geophys. Res. Lett., 29, 20
Kepko L., Spence H. E., 2003, J. Geophys. Res., 108, 1257
Kohl J. L. et al., 1997, Sol. Phys., 175, 613
Krieger A. S., Timothy A. F., Roelof E. C., 1973, Sol. Phys., 29, 505
Landi E., Alexander R. L., Gruesbeck J. R., Gilbert J. A., Lepri S. T., Manchester W. B., Zurbuchen T. H., 2012, ApJ, 744, 100
Lazarus A., Kasper J., Szabo A., Ogilvie K., 2003, in Velli M., Bruno R., Malara F., eds, AIP Conf. Proc. Vol. 679, Solar Wind Ten: Proceedings of the Tenth International Solar Wind Conference. Am. Inst. Phys., New York, p. 187
Levine R. H., Altschuler M. D., Harvey J. W., 1977, J. Geophys. Res., 82, 1061
Liu Y., Richardson J., Belcher J., 2005, Planet. Space Sci., 53, 3
McGregor S. L., Hughes W. J., Arge C. N., Odstrcil D., Schwadron N. A., 2011, J. Geophys. Res.: Space Phys., 116, A03106
Marsch E., Mühlhäuser K.-H., Rosenbauer H., Schwenn R., Denskat K. U., 1981, J. Geophys. Res., 86, 9199
Marsch E., Mühlhäuser K.-H., Rosenbauer H., Schwenn R., Neubauer F. M., 1982a, J. Geophys. Res., 87, 35
Marsch E., Mühlhäuser K.-H., Schwenn R., Rosenbauer H., Pilipp W., Neubauer F. M., 1982b, J. Geophys. Res., 87, 52
Marsch E., Ao X.-Z., Tu C.-Y., 2004, J. Geophys. Res.: Space Phys., 109, A04102
Maruca B. A., Kasper J. C., Bale S. D., 2011, Phys. Rev. Lett., 107, 201101
Matteini L., Landi S., Hellinger P., Pantellini F., Maksimovic M., Velli M., Goldstein B. E., Marsch E., 2007, Geophys. Res. Lett., 34, L20105
Matteini L., Hellinger P., Landi S., Trávníček P. M., Velli M., 2011, Space Sci. Rev., 172, 373
Matteini L., Horbury T. S., Pantellini F., Velli M., Schwartz S. J., 2015, ApJ, 802, 11
Müller D., Marsden R. G., St. Cyr O. C., Gilbert H. R., 2013, Sol. Phys., 285, 25
Musmann G., Neubauer F. M., Maier A., Lammers E., 1975, Raumfahrtforschung, 19, 232
Neugebauer M. et al., 1998, J. Geophys. Res.: Space Phys., 103, 14587
Neugebauer M., Liewer P. C., Smith E. J., Skoug R. M., Zurbuchen T. H., 2002, J. Geophys. Res.: Space Phys., 107, 1488
Neugebauer M., Reisenfeld D., Richardson I. G., 2016, J. Geophys. Res.: Space Phys., 121, 8215
Pagel A. C., Crooker N. U., Zurbuchen T. H., Gosling J. T., 2004, J. Geophys. Res.: Space Phys., 109, A01113
Peleikis T., Kruse M., Berger L., Wimmer-Schweingruber R., 2017, A&A, 602, A24
Phillips J. L. et al., 1995, Geophys. Res. Lett., 22, 3301
Pinto R. F., Brun A. S., Rouillard A. P., 2016, A&A, 592, A65
Pizzo V. J., 1991, J. Geophys. Res., 96, 5405
Richardson I. G., 2018, Living Rev. Sol. Phys., 15, 1
Roberts D. A., Goldstein M. L., Klein L. W., Matthaeus W. H., 1987, J. Geophys. Res., 92, 12023
Rosenbauer H., Schwenn R., Miggenrieder H., Meyer B., Gründwaldt H., Mühlhäuser K.-H., Pellkofer H., Wolfe J. H., 1981, Helios E1 (Plasma) Instrument Technical Document.
Rouillard A. P. et al., 2010, J. Geophys. Res.: Space Phys., 115, A04104
Sanchez-Diaz E., Rouillard A. P., Davies J. A., Lavraud B., Pinto R. F., Kilpua E., 2017, ApJ, 851, 32
Scearce C., Cantarano S., Ness N., Mariani F., Terenzi R., Burlaga L., 1975, Raumfahrtforschung, 19, 237
Schwenn R., 2007, Space Sci. Rev., 124, 51
Schwenn R., Rosenbauer H., Miggenrieder H., 1975, Raumfahrtforschung, 19, 226
Sheeley N. R., Harvey J. W., Feldman W. C., 1976, Sol. Phys., 49, 271
Sheeley N. R. et al., 1997, ApJ, 484, 472
Slemzin V., Harra L., Urnov A., Kuzin S., Goryaev F., Berghmans D., 2013, Sol. Phys., 286, 157
Sonnerup B. U. Ö., Papamastorakis I., Paschmann G., Lühr H., 1987, J. Geophys. Res., 92, 12137

Stakhiv M., Lepri S. T., Landi E., Tracy P., Zurbuchen T. H., 2016, ApJ, 829, 117
Stansby D., Horbury T. S., 2018, A&A, 613, A62
Stansby D., Salem C. S., Matteini L., Horbury T. S., 2018a, preprint (arXiv:1807.04376)
Stansby D., Yatharth Shaw S., 2018b, Heliopython/Heliopy: HelioPy 0.5.3. Available at: https://zenodo.org/record/1309004
Steinberg J. T., Lazarus A. J., Ogilvie K. W., Lepping R., Byrnes J., 1996, Geophys. Res. Lett., 23, 1183
Susino R., Ventura R., Spadaro D., Vourlidas A., Landi E., 2008, A&A, 488, 303
Thieme K., Schwenn R., Marsch E., 1989, Adv. Space Res., 9, 127
Viall N. M., Vourlidas A., 2015, ApJ, 807, 176
Wang Y.-M., 2010, ApJ, 715, L121
Wang Y.-M., Sheeley N. R. J., 1990, ApJ, 355, 726
Wang Y.-M., Sheeley N. R., 1991, ApJ, 372, L45
Wang Y.-M., Ko Y.-K., Grappin R., 2009, ApJ, 691, 760
Wimmer-Schweingruber R. F., von Steiger R., Paerli R., 1997, J. Geophys. Res.: Space Phys., 102, 17407
Xu F., Borovsky J. E., 2015, J. Geophys. Res.: Space Phys., 120, 70
Yoon P. H., 2016, J. Geophys. Res.: Space Phys., 121, 665
Zhao L., Zurbuchen T. H., Fisk L. A., 2009, Geophys. Res. Lett., 36, L14104
Zhao L., Landi E., Lepri S. T., Gilbert J. A., Zurbuchen T. H., Fisk L. A., Raines J. M., 2017, ApJ, 846, 135
Zurbuchen T. H., Fisk L. A., Gloeckler G., von Steiger R., 2002, Geophys. Res. Lett., 29, 1352

This paper has been typeset from a TEX/LATEX file prepared by the author.

List of astronomical key words (Updated on 2017 March)

This list is common to *Monthly Notices of the Royal Astronomical Society, Astronomy and Astrophysics*, and *The Astrophysical Journal*. In order to ease the search, the key words are subdivided into broad categories. No more than *six* subcategories altogether should be listed for a paper.

The subcategories in boldface containing the word 'individual' are intended for use with specific astronomical objects; these should never be used alone, but always in combination with the most common names for the astronomical objects in question. Note that each object counts as one subcategory within the allowed limit of six.

The parts of the key words in italics are for reference only and should be omitted when the keywords are entered on the manuscript.

General
editorials, notices
errata, addenda
extraterrestrial intelligence
history and philosophy of astronomy
miscellaneous
obituaries, biographies
publications, bibliography
sociology of astronomy
standards

Physical data and processes
acceleration of particles
accretion, accretion discs
asteroseismology
astrobiology
astrochemistry
astroparticle physics
atomic data
atomic processes
black hole physics
chaos
conduction
convection
dense matter
diffusion
dynamo
elementary particles
equation of state
gravitation
gravitational lensing: micro
gravitational lensing: strong
gravitational lensing: weak
gravitational waves
hydrodynamics
instabilities
line: formation
line: identification
line: profiles
magnetic fields
magnetic reconnection
(magnetohydrodynamics) MHD
masers
molecular data
molecular processes
neutrinos
nuclear reactions, nucleosynthesis, abundances
opacity
plasmas
polarization
radiation: dynamics
radiation mechanisms:general
radiation mechanisms: non-thermal
radiation mechanisms: thermal
radiative transfer
relativistic processes
scattering
shock waves
solid state: refractory
solid state: volatile
turbulence
waves

Astronomical instrumentation, methods and techniques
atmospheric effects
balloons
instrumentation: adaptive optics
instrumentation: detectors
instrumentation: high angular resolution
instrumentation: interferometers
instrumentation: miscellaneous
instrumentation: photometers
instrumentation: polarimeters
instrumentation: spectrographs
light pollution
methods: analytical
methods: data analysis
methods: laboratory: atomic
methods: laboratory: molecular
methods: laboratory: solid state
methods: miscellaneous
methods: numerical
methods: observational
methods: statistical
site testing
space vehicles
space vehicles: instruments
techniques: high angular resolution
techniques: image processing
techniques: imaging spectroscopy
techniques: interferometric
techniques: miscellaneous
techniques: photometric
techniques: polarimetric
techniques: radar astronomy
techniques: radial velocities
techniques: spectroscopic
telescopes

Astronomical data bases
astronomical data bases: miscellaneous
atlases
catalogues
surveys
virtual observatory tools

Astrometry and celestial mechanics
astrometry
celestial mechanics
eclipses
ephemerides
occultations
parallaxes
proper motions
reference systems
time

The Sun
Sun: abundances
Sun: activity
Sun: atmosphere
Sun: chromosphere
Sun: corona
Sun: coronal mass ejections (CMEs)
Sun: evolution
Sun: faculae, plages
Sun: filaments, prominences
Sun: flares
Sun: fundamental parameters
Sun: general
Sun: granulation
Sun: helioseismology
Sun: heliosphere
Sun: infrared
Sun: interior
Sun: magnetic fields
Sun: oscillations
Sun: particle emission
Sun: photosphere
Sun: radio radiation
Sun: rotation
(Sun:) solar–terrestrial relations
(Sun:) solar wind
(Sun:) sunspots
Sun: transition region
Sun: UV radiation
Sun: X-rays, gamma-rays

Planetary systems
comets: general

comets: individual: . . .
Earth
interplanetary medium
Kuiper belt: general

Kuiper belt objects: individual: . . .
meteorites, meteors, meteoroids
minor planets, asteroids: general

minor planets, asteroids: individual: . . .
Moon
Oort Cloud
planets and satellites: atmospheres
planets and satellites: aurorae
planets and satellites: composition
planets and satellites: detection
planets and satellites: dynamical evolution and stability
planets and satellites: formation
planets and satellites: fundamental parameters
planets and satellites: gaseous planets
planets and satellites: general

planets and satellites: individual: . . .
planets and satellites: interiors
planets and satellites: magnetic fields
planets and satellites: oceans
planets and satellites: physical evolution
planets and satellites: rings
planets and satellites: surfaces
planets and satellites: tectonics
planets and satellites: terrestrial planets
planet–disc interactions
planet–star interactions
protoplanetary discs
zodiacal dust

Stars
stars: abundances
stars: activity
stars: AGB and post-AGB
stars: atmospheres
(stars:) binaries *(including multiple)*: close
(stars:) binaries: eclipsing
(stars:) binaries: general
(stars:) binaries: spectroscopic
(stars:) binaries: symbiotic
(stars:) binaries: visual
stars: black holes
(stars:) blue stragglers
(stars:) brown dwarfs
stars: carbon
stars: chemically peculiar
stars: chromospheres
(stars:) circumstellar matter
stars: coronae
stars: distances
stars: dwarf novae
stars: early-type
stars: emission-line, Be
stars: evolution
stars: flare
stars: formation
stars: fundamental parameters
(stars:) gamma-ray burst: general
(stars:) **gamma-ray burst: individual: . . .**
stars: general
(stars:) Hertzsprung–Russell and colour–magnitude diagrams
stars: horizontal branch
stars: imaging
stars: individual: . . .
stars: interiors

stars: jets
stars: kinematics and dynamics
stars: late-type
stars: low-mass
stars: luminosity function, mass function
stars: magnetars
stars: magnetic field
stars: massive
stars: mass-loss
stars: neutron
(stars:) novae, cataclysmic variables
stars: oscillations *(including pulsations)*
stars: peculiar *(except chemically peculiar)*
(stars:) planetary systems
stars: Population II
stars: Population III
stars: pre-main-sequence
stars: protostars
(stars:) pulsars: general
(stars:) **pulsars: individual: . . .**
stars: rotation
stars: solar-type
(stars:) starspots
stars: statistics
(stars:) subdwarfs
(stars:) supergiants
(stars:) supernovae: general
(stars:) **supernovae: individual: . . .**
stars: variables: Cepheids
stars: variables: Scuti
stars: variables: general
stars: variables: RR Lyrae
stars: variables: S Doradus
stars: variables: T Tauri, Herbig Ae/Be
(stars:) white dwarfs
stars: winds, outflows
stars: Wolf–Rayet

Interstellar medium (ISM), nebulae
ISM: abundances
ISM: atoms
ISM: bubbles
ISM: clouds
(ISM:) cosmic rays
(ISM:) dust, extinction
ISM: evolution
ISM: general
(ISM:) HII regions
(ISM:) Herbig–Haro objects

ISM: individual objects: . . .
(except planetary nebulae)
ISM: jets and outflows
ISM: kinematics and dynamics
ISM: lines and bands
ISM: magnetic fields
ISM: molecules
(ISM:) photodissociation region (PDR)
(ISM:) planetary nebulae: general
(ISM:) **planetary nebulae: individual: . . .**
ISM: structure
ISM: supernova remnants

The Galaxy
Galaxy: abundances
Galaxy: bulge
Galaxy: centre
Galaxy: disc
Galaxy: evolution
Galaxy: formation
Galaxy: fundamental parameters
Galaxy: general
(Galaxy:) globular clusters: general
(Galaxy:) **globular clusters: individual: . . .**
Galaxy: halo
Galaxy: kinematics and dynamics
(Galaxy:) local interstellar matter
Galaxy: nucleus
(Galaxy:) open clusters and associations: general
(Galaxy:) **open clusters and associations: individual: . . .**
(Galaxy:) solar neighbourhood
Galaxy: stellar content
Galaxy: structure

Galaxies
galaxies: abundances
galaxies: active
(galaxies:) BL Lacertae objects: general
(galaxies:) **BL Lacertae objects: individual: . . .**
galaxies: bulges
galaxies: clusters: general

galaxies: clusters: individual: . . .
galaxies: clusters: intracluster medium
galaxies: distances and redshifts
galaxies: dwarf
galaxies: elliptical and lenticular, cD
galaxies: evolution
galaxies: formation
galaxies: fundamental parameters
galaxies: general
galaxies: groups: general

galaxies: groups: individual: . . .
galaxies: haloes
galaxies: high-redshift

galaxies: individual: . . .
galaxies: interactions
(galaxies:) intergalactic medium
galaxies: irregular
galaxies: ISM
galaxies: jets
galaxies: kinematics and dynamics
(galaxies:) Local Group
galaxies: luminosity function, mass function
(galaxies:) Magellanic Clouds
galaxies: magnetic fields
galaxies: nuclei
galaxies: peculiar
galaxies: photometry
(galaxies:) quasars: absorption lines
(galaxies:) quasars: emission lines
(galaxies:) quasars: general

(galaxies:) **quasars: individual: . . .**
(galaxies:) quasars: supermassive black holes
galaxies: Seyfert
galaxies: spiral
galaxies: starburst
galaxies: star clusters: general

galaxies: star clusters: individual: . . .
galaxies: star formation
galaxies: statistics
galaxies: stellar content
galaxies: structure

Cosmology
(cosmology:) cosmic background radiation
(cosmology:) cosmological parameters
(cosmology:) dark ages, reionization, first stars
(cosmology:) dark energy
(cosmology:) dark matter
(cosmology:) diffuse radiation
(cosmology:) distance scale
(cosmology:) early Universe
(cosmology:) inflation
(cosmology:) large-scale structure of Universe
cosmology: miscellaneous
cosmology: observations
(cosmology:) primordial nucleosynthesis
cosmology: theory

Resolved and unresolved sources as a function of wavelength
gamma-rays: diffuse background
gamma-rays: galaxies
gamma-rays: galaxies: clusters
gamma-rays: general
gamma-rays: ISM
gamma-rays: stars
infrared: diffuse background
infrared: galaxies
infrared: general
infrared: ISM
infrared: planetary systems
infrared: stars
radio continuum: galaxies
radio continuum: general
radio continuum: ISM
radio continuum: planetary systems
radio continuum: stars
radio continuum: transients
radio lines: galaxies
radio lines: general
radio lines: ISM
radio lines: planetary systems
radio lines: stars
submillimetre: diffuse background
submillimetre: galaxies
submillimetre: general
submillimetre: ISM
submillimetre: planetary systems
submillimetre: stars
ultraviolet: galaxies
ultraviolet: general
ultraviolet: ISM
ultraviolet: planetary systems
ultraviolet: stars
X-rays: binaries
X-rays: bursts
X-rays: diffuse background
X-rays: galaxies
X-rays: galaxies: clusters
X-rays: general
X-rays: individual: . . .
X-rays: ISM
X-rays: stars